Wetting and Dewetting of Complex Surface Geometries

Stephan Herminghaus,[1] Martin Brinkmann,[1] and Ralf Seemann[1,2]

[1]Max-Planck Institute for Dynamics and Self-Organization, D 37073 Göttingen, Germany;
email: stephan.herminghaus@ds.mpg.de

[2]Experimental Physics, Saarland University, D 66123 Saarbrücken, Germany

Key Words

structure formation, microfluidics, biomimetic systems, interfaces

Abstract

Surfaces exhibiting complex topographies, such as those encountered in biology, give rise to an enormously rich variety of interfacial morphologies of a liquid to which they are exposed. In the present article, we elaborate on some basic mechanisms involved in the statics and dynamics of such morphologies, focusing on a few simple paradigm topographies. We demonstrate that different liquid interface morphologies on the same sample frequently coexist. To exemplify the impact of the dynamics on the final droplet morphology, we discuss the shape instability of filamentous liquid structures in wedge geometries. We finally show that some side effects that may dominate on a larger scale, such as contact line pinning and contact angle hysteresis, seem to play a minor role on the microscopic scale under study. This establishes the validity of simple theoretical concepts of wetting as a starting point for describing liquids at substrate surfaces of high complexity.

1. INTRODUCTION

Solid surfaces decorated with complex surface geometries can exhibit unusual wetting properties. On the one hand, the surface of a moderately hydrophobic material can become highly water repellent when decorated with a pattern of microscopic pillars (1–3). On the other hand, liquids can spontaneously organize into a large variety of different droplet shapes in the presence of surface topographies during condensation or dewetting (4–8). This is particularly important in the case of biological surfaces, which are often equipped with a complex texture of hydrophobic microstructures. The most prominent example is the superhydrophobic Lotus leaf, which is covered with hierarchies of bumps (papillae) made of epicuticular wax (1). Similar structures are found on many other plants, e.g., quite common ones such as the Indian Cress (9), or on insect wings (10). Some lichen species use hydrophobic crystals attached to their surface as a protection against imbibition of rain water (11, 12). Hairy structures on the legs of a water strider induce a strong water repellency and allow the animal to "walk" on water (13). These examples underline the universality of complex surface topographies as a means to achieve hydrophobicity in Nature (2).

The tremendous variety of structures involved in these surface systems, ranging from the submicrometer to the millimeter range, makes very difficult a concise treatment of the basic mechanisms governing the various wetting phenomena observed on such surfaces. Some aspects of these systems have already been successfully imitated in generating artificial superhydrophobic surfaces (14), and some very prominent effects have been demonstrated with a roughness on a well-defined scale (15, 16). However, the microscopic physics occurring on the scale of the individual protrusions and troughs has been only occasionally addressed. In the present paper, we therefore focus on the statics as well as the dynamics of wetting of a few simple, paradigmatic topographic features. These simple structures unfold such a rich spectrum of phenomena that a full understanding of wetting at biological surfaces remains a formidable but potentially rewarding task.

2. WETTING OF SOLID SUBSTRATES

Most structures found on biological surfaces are on a submillimeter length scale. In that regime, the statics and dynamics of a liquid in contact with such surfaces are governed solely by interfacial tensions, and gravity can be safely neglected. One may regard the wetting liquid as being nonvolatile as long as the typical timescale of a measurement is smaller than the timescales of evaporation or condensation. This implies that static droplet configurations represent local minima of the interfacial free energy for a fixed liquid volume (17).

If, however, the length scale of the wetting liquid is on the nanometer scale or smaller, chemical equilibration of the liquid and its surrounding vapor phase is fast, on the timescale of a measurement (18, 19). In this case, the supersaturation of the vapor phase represents a suitable control parameter of the system (20, 21). The Kelvin equation establishes a direct relation between the supersaturation and the difference between the actual chemical potential and the chemical potential at bulk coexistence (20–22).

The interfacial tension between two bulk phases equals the (reversible) work per surface area required to enlarge the interface. Thus, an alternative definition of the interfacial tension is the excess free energy of the interface with respect to the bulk free energy of the adjacent phases (22). Thermodynamic stability requires the surface tension of the liquid-vapor interface to be positive. Its value can be estimated from the average area of a molecule in the interface and the work required to bring a molecule from the bulk to the interface.

Details of the molecular interactions, however, are not relevant on length scales larger than this microscopic length for which the spatial configuration of the free liquid interface comprises the relevant information about the system. Within the capillary model, all interfaces are regarded as mathematical surfaces, i.e., ideal interfaces of zero width. The three-phase region, in which the wetting liquid, the ambient fluid phase, and the solid meet, is modeled as a three-dimensional curve lying in the surface of the solid.

Long-range interactions like van der Waals or electrostatic forces can be easily built into the capillary model in the form of a local pressure contribution (disjoining pressure) acting on the liquid-vapor interface (23). These type of models have been successfully applied to describe the dewetting dynamics of thin liquid films (24, 25), liquids adsorbed to chemically heterogeneous solid substrates (26), or the stability and internal structure of the contact line (27). Contributions of the disjoining pressure to the total pressure of the liquid come into play if the thickness of the wetting layer is less than roughly 100 nm (17–19, 28). So far, the intrinsic width of the interface and the interfacial roughness caused by thermal fluctuations are still orders of magnitude smaller than the size of the smallest liquid droplets observed in experiments (18, 19, 28, 29).

In the remainder of this article we discuss the wetting of solids decorated with complex surface geometries in the range of micrometers or larger. The capillary model applies to these systems without further restrictions. In Subsections 2.1 and 2.2 we give a short overview of the mechanical equilibrium conditions derived within the capillary model and address the pinning of the three-phase line to surface topographies.

2.1. Equilibrium Conditions

The local mechanical equilibrium between the liquid-vapor interface and its adjacent bulk phases is expressed by the Laplace equation

$$\Delta P = 2H\gamma, \qquad\qquad 1.$$

relating the pressure difference ΔP across the liquid-vapor interface to its mean curvature H and interfacial tension γ (for a mathematical definition of the mean curvature H, see, for instance, Reference 30). For length scales smaller than the capillary length,

$$\ell_c = \sqrt{\frac{\gamma}{g|\Delta\rho|}}, \qquad\qquad 2.$$

where $l_c \approx 2.7$ mm for water, one may neglect contributions of the hydrostatic pressure to the Laplace pressure ΔP. Here, $\Delta\rho$ denotes the difference of fluid densities, and g is the acceleration of gravity. Contributions of the disjoining pressure become virtually unnoticeable if the droplet height exceeds a microscopic length ℓ_m that is ≈ 100 nm (18, 19, 28). In this broad range of length scales between ℓ_c and ℓ_m, which spans more than four orders of magnitude, the free liquid interface of a static droplet is a surface of constant mean curvature (17).

On an ideally smooth and chemically homogeneous solid surface, a liquid droplet assumes the shape of a spherical cap after mechanical equilibration. The contact angle θ, i.e., the slope of the static liquid-vapor interface at the (ideal) solid, satisfies the equation of Young and Dupré:

$$\gamma \cos\theta = \gamma_{sv} - \gamma_{sl}, \qquad\qquad 3.$$

where γ_{sv} and γ_{sl} denote the surface tensions of the vapor-solid interface and the liquid-solid interface, respectively. This highly idealized situation is nearly matched only in experiments on thoroughly cleaned and smooth substrates. For the vast majority of solid surfaces, the apparent contact angle of a wetting droplet depends on the history of preparation, i.e., whether the contact line was advancing or receding before the liquid-vapor interface reached a static configuration.

The hysteresis of the apparent contact angle, and thus of the whole droplet shape, can be explained from the highly corrugated energy landscape in the presence of either topographic or chemical heterogeneities on the solid surface (23). The equation of Young and Dupré (Equation 3) is still valid on a length scale below the typical dimensions of the topographies or the chemical heterogeneities. As a result of these surface imperfections, or defects, the liquid-vapor interface will be trapped in one out of a large number of possible metastable equilibria and may be far from the optimal energetic configuration.

2.2. Equations of Wenzel and Cassie

Cassie (31) was the first to consider the apparent contact angle of a droplet in the energetically optimal droplet configuration wetting a plane and chemically heterogeneous surface. Shortly after Cassie, Wenzel (32) treated the analogous problem for a droplet wetting a rough but chemically homogeneous substrate. In both cases, the diameter of the surface being wet by liquid has to be much larger than the typical size of the heterogeneities or topographies.

Cassie's law states that the apparent contact angle, θ_0, of the optimal droplet configuration wetting a plane substrate with patches $i = 1, \ldots, N$ of different wettability is given by

$$\cos \theta_0 = \sum_{i=1}^{N} \phi_i \cos \theta_i, \qquad 4.$$

where θ_i is Young's contact angle on a homogeneous patch i. In Equation 4, the cosine of Young's angles is weighted by the fraction $\phi_i \equiv A_i / \sum_{i=1}^{N} A_i$ of their surface area A_i. Swain & Lipowsky (33) have proposed alternative weights by the length of the contact line.

In the same spirit of the above Cassie's equation, Wenzel derived an analogous relation,

$$\cos \theta_0 = r \cos \theta, \qquad 5.$$

relating the cosine of the apparent contact angle to Young's contact angle θ and the ratio $r \equiv A/A_0$ of the true surface area, A, to the total base area of the substrate, A_0 (32).

2.3. Contact Line Pinning

The key to understanding the large spectrum of different liquid morphologies on surfaces with complex surface geometries lies in the behavior of the three-phase contact line (4–6, 8, 34, 35). As mentioned in Subsection 2.1, above, the equation of Young and Dupré (4) is valid only if the contact line is located on a smooth part of the surface. Kinks in the surface topography, i.e., acute edges, have the ability to immobilize the contact line. If the slope of the free liquid interface at the contact line falls into an interval limited by the slopes with respect to the equilibrium positions to one or the other side of the kink, the contact line will be trapped in such a "pinned" state (16, 23). This situation is illustrated in **Figure 1** in a plane cut perpendicular to the contact line. Ondarcuhu & Piednoir (36) show that the threshold height of a step to cause contact line pinning of a dewetting polymer film is on the order of only a few nanometers.

Pinning the contact line by means of surface topographies opens new degrees of freedom for the liquid-vapor interface in equilibrium. As we illustrate in Section 4, contact line pinning is responsible for the rich spectrum of static droplet shapes on topographically structured substrates. But not only the equilibrium is affected by contact line pinning: The dewetting dynamics of filamentous liquid structures in linear surface grooves is substantially different for laterally pinned and nonpinned contact lines. This phenomenon has strong implications for the liquid pattern after dewetting and for the final droplet morphology.
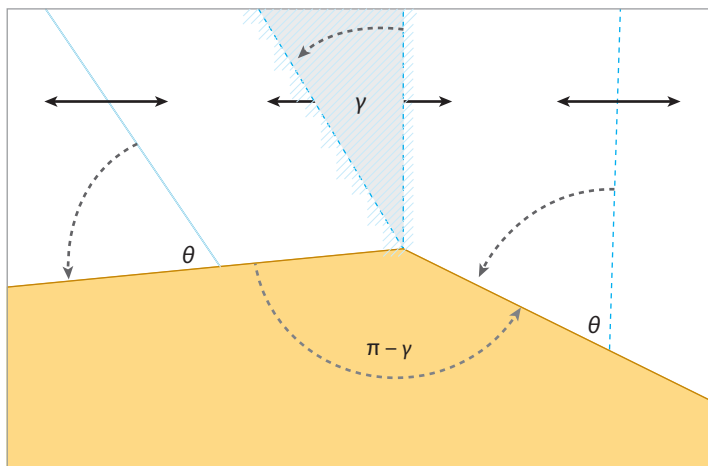
Figure 1

Contact line pinning at an ideal acute edge. In the pinned state, the slope of the liquid-vapor interface lies in the hatched sector of width γ, where $\pi - \gamma$ is the opening angle of the solid wedge.

2.4. Computation of Droplet Shapes

On the submillimeter length scale down to the size of few hundred nanometers, the liquid-vapor interface of a liquid wetting a solid substrate has to be a surface of constant mean curvature in equilibrium (17). This allows one to construct possible equilibria of the liquid-vapor interface from surfaces of constant mean curvature whose shape can be explicitly parameterized. The slope of such a surface at the contact line or, to be precise, the local contact angle θ has to satisfy the equation of Young and Dupré (4) on smooth parts of the surface and to be consistent with the conditions of pinning wherever the contact line coincides with an acute kink of the surface. However, only a few substrate geometries of high symmetry allow such an explicit construction of static droplet shapes. Even for simple surface geometries, like a topographic step or linear channels with rectangular cross section, analytical solutions are not feasible (4, 35).

Approximations of the liquid shapes through simple surfaces of constant mean curvature can lead to asymptotically exact results. A meaningful approximation requires that the equilibrium condition be matched in most parts of the contact line. An illustrative example is given by liquid filaments of finite length wetting linear topographies of various cross sections, as discussed in more detail in Section 4.2. Aside from small regions close to either end, the liquid-vapor interface of a filament can be well approximated by a segment of a cylinder whose axis lies parallel to the direction of the groove (4, 6, 35). Errors in volume or interfacial free energy will be small if the extension of the liquid filament into the direction of the grooves is larger than a few times of the groove width (6).

Rather than the use of surfaces of constant mean curvature, the liquid-vapor interface may be represented by a mesh of small triangles spanning neighboring nodes. Numerical minimizations of the interfacial energy yield the static droplet shapes as local minima. The shape of the free liquid interface may undergo large changes during a minimization that is accompanied by large dilations and compressions of the mesh. These deformations necessitate a "surface surgery" to keep the quality of the mesh in the desired range. This is reached by changes in the local topology of the triangular mesh through edge flipping. Edges whose length does not fall into the desired range are constantly refined or removed from the surface. Numerical minimizations using such dynamically triangulated surfaces can be performed, for example, with the freely available software

Surface Evolver, developed by Brakke (37, 38). By the use of individual scripts, this software can be adapted to a large variety of surface geometries (8, 35). Its script language offers a spectrum of methods to extract relevant quantities like the actual Laplace pressure of the droplet or the positions of particular points of the contact line from the numerical model.

3. PREPARATION OF SURFACE TOPOGRAPHIES

Surfaces with regular arrays of simple geometric motives such as linear grooves or posts, as well as irregular structures, e.g., carpets of small crystalline aggregates, can be created in a large range of lateral dimensions. Facing the rich and diverse literature published over the past decade, here we merely give a short overview of the most common and established techniques employed in the context of fundamental research.

Large topographic structures in metal or polymeric material with dimensions down to approximately 100-μm width can be micromachined (39–43). This technique covers a wide spectrum of surface geometries. Its major disadvantage is the large roughness of the machined surfaces, which creates a large contact angle hysteresis.

Imprinting or embossing of surface topographies into molten polymeric material or curable prepolymers is advantageous if larger numbers of identical substrates are needed (44–51). These techniques require larger efforts to fabricate a suitable master that must be made by the use of a robust material like glass or silicon. In a similar fashion, topographic structures of the same length scales can be produced from polymeric materials by soft lithography, in which silicon rubber molds instead of rigid ones are used (52–54). The surface roughness of the samples is typically small and mostly determined by the quality of the master. Hence, substrates fabricated with imprinting and embossing are well suited for wetting experiments and can be produced in larger amounts.

Some experiments, in particular those in fundamental research, necessitate a gradual variation of the surface geometry between different samples such as a variation of the aspect ratio, cross section of the structures, or lattice spacing in a periodic pattern. The aspect ratio X is defined as the ratio of the depth, h, to a typical width w of the geometry. This gradual variation can be achieved with standard photolithography techniques (55) and subsequent dry- or wet-etching procedures (4, 7, 15, 34, 56, 57). In most situations, glass and silicon are suitable substrate materials. Well-defined small-scale geometries with triangular or trapezoidal cross sections can be fabricated by wet etching of monocrystalline silicon substrates with KOH (5, 6, 56). The etched walls form an angle of 54.7° with the (1, 0, 0) surface of the silicon crystal. Isotropic reactive (dry) etching, however, leads to rectangular cross sections that can have very high aspect ratios (4, 57). Glass or silicon substrates can be grafted with self-assembling monolayers (SAMs) that modify the wettability of the surfaces. Contact angle hysteresis on surfaces covered by SAMs is typically small, indicating chemical homogeneity and a low surface roughness.

Specific liquid morphologies on topographically structured substrates are created either by dip coating (55) or by melting of a film of polymeric material (5), or through condensation of liquid from a vapor phase onto the sample surface (4, 6, 7, 34). A three-dimensional analysis of the emerging liquid morphologies requires refined imaging techniques. Liquids that can be solidified after preparation are highly favorable for most of these techniques (4, 54). This holds for atomic force microscopy (AFM), scanning probe microscopy (SPM), or scanning electron microscopy (SEM).

Lateral compression of polydimethylsiloxane elastomer (PDMS) surfaces after treatment with UV light and ozone leads to a wrinkling instability of the surface (58). The wrinkle pattern exhibits a sinusoidal cross section and shows a constant periodicity over many periods. This technique allows an active control of the surface geometry because the formation of wrinkles is fully reversible. The development of cracks, however, poses a limit to the degree of compression (58).

Surfaces with a random topography on two length scales similar to those found in nature can be created through controlled self-assembly of small silica beads grafted onto larger silica beads (59). The shape of these resulting composite particles resembles that of a raspberry. After grafting of PDMS onto the silica beads, a monolayer of these composite particles exhibits a pronounced superhydrophobic effect (59).

4. WETTING OF LINEAR TOPOGRAPHIES

As mentioned in the Introduction (Section 1), this article focuses on the wetting and dewetting in the presence of paradigmatic surface topographies of high symmetry. Linear surface grooves with a polygonal cross section provide a promising starting point. We demonstrate in this section that the spectrum and complexity of static wetting morphologies in grooves of polygonal cross section are directly linked to the number of kinks.

4.1. Solid Wedge and Topographic Step

The most fundamental effectively one-dimensional substrate geometry is an infinite wedge formed by two intersecting planes. Because of its invariance with respect to rescaling in all dimensions, an infinite wedge has no intrinsic length scale and is completely characterized by the angle α between the plane walls. In the remainder of this article we make use of the wedge angle $\psi = 90° - \alpha/2$, as shown in **Figure 2c**. Because the liquid volume of a droplet wetting such an ideal infinite wedge can always be rescaled to unity, we are left with the contact angle θ and the wedge angle ψ as the only relevant parameters governing the appearance of different droplet shapes in equilibrium.

Figure 3 depicts the two static liquid morphologies found in a wedge: (*a*) droplets with a liquid-vapor interface given by a segment of a sphere and (*b*) infinitely long liquid filaments of homogeneous cross section. The free liquid interface of the latter is cylindrical and always curved
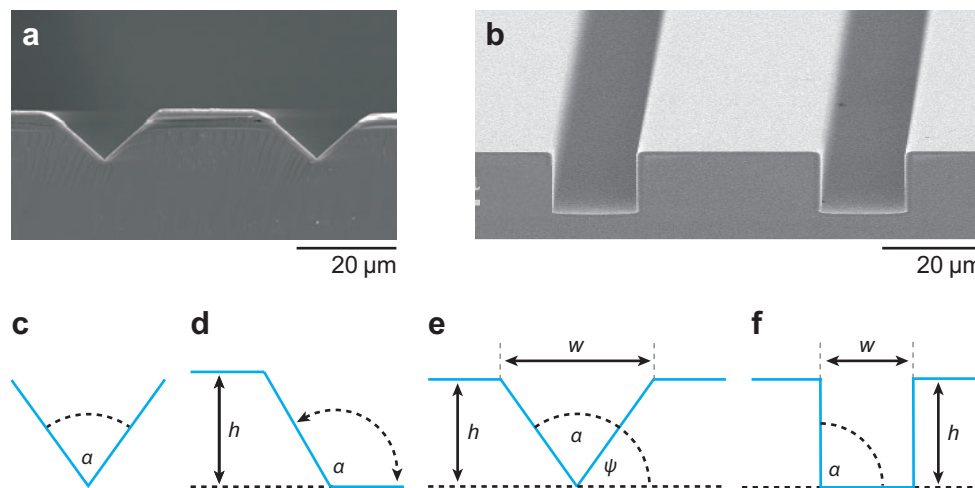
Figure 2

(*Top row*) SEM images of cuts through etched silicon substrates with triangular grooves (*a*) and rectangular grooves (*b*). (*Bottom row*) A variety of possible polygonal cross sections for linear surface topographies: (*c*) an infinite wedge, (*d*) a topographic step, (*e*) grooves with triangular cross section, and (*f*) grooves with trapezoidal cross section.
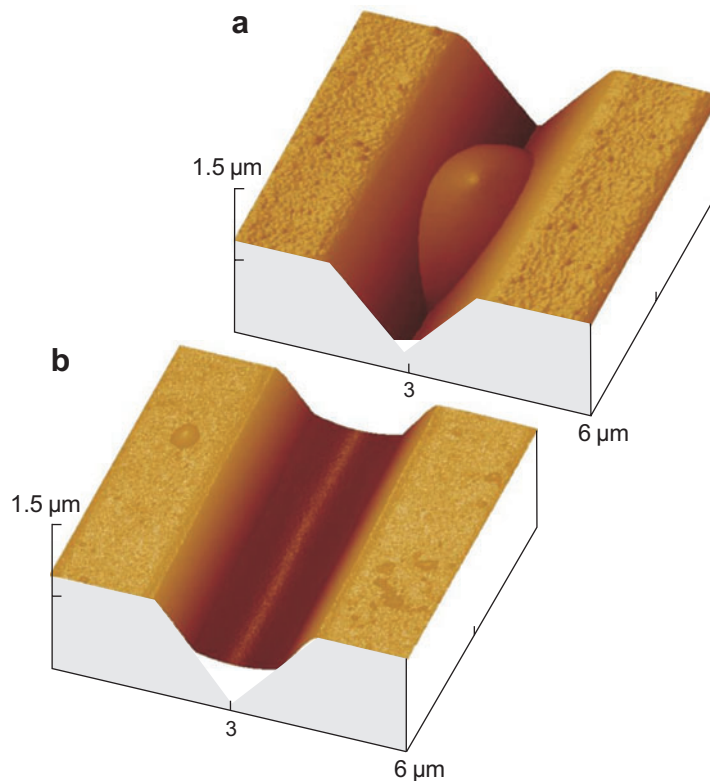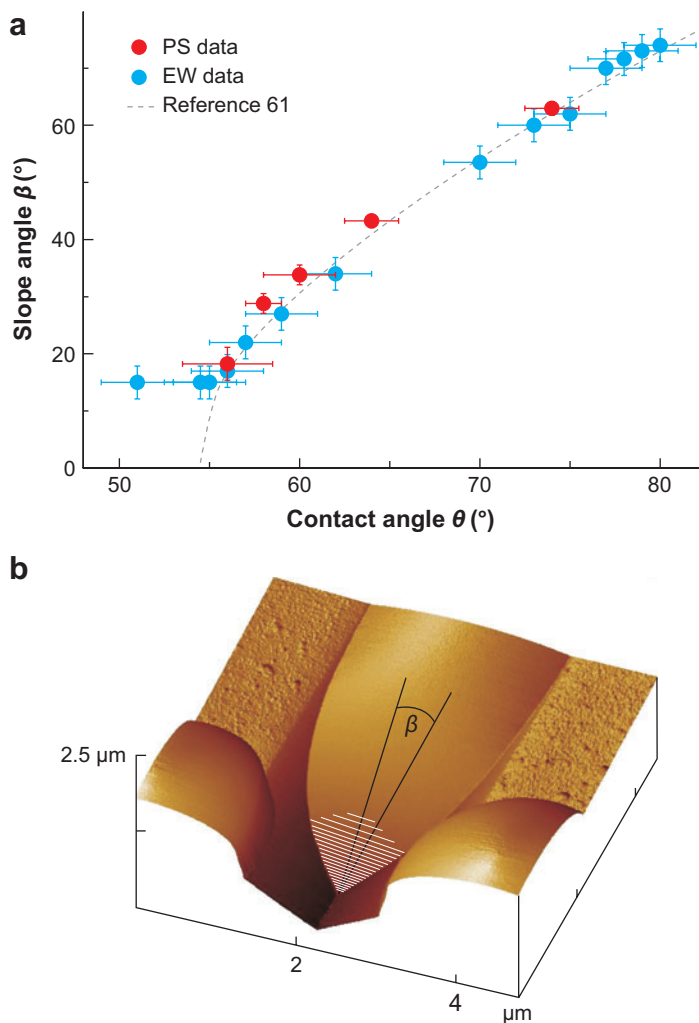
Figure 3

AFM micrographs of polystyrene morphologies in a wedge with an opening angle $\theta = 54.7°$. The wettability of the silicon substrate has been modified through the use of different self-assembling monolayers (SAMs). (*a*) Spherical droplet for $\theta \approx 64°$. (*b*) Liquid filament with negative Laplace pressure for $\theta \approx 33°$.

toward the substrate. In the particular situation shown in **Figure 3**, the triangular groove of finite width can be regarded as virtually infinite because the liquid does not explore the upper edge of the groove. A finite curvature of the wedge bottom breaks the scaling invariance and, thus, introduces a length scale to the system (60).

The appearance of these morphologies is governed solely by the equilibrium contact angle θ and the wedge angle ψ. Spherical droplets appear for $\theta > \psi$, whereas liquid filaments are found for contact angles $\theta < \psi$. In the limit of θ approaching ψ from below, such a stable liquid filament develops a whole spectrum of soft deformation modes. Thus, the shape of the filament becomes susceptible to fluctuations that can be caused either by random disorder or by thermal noise (20, 21). In the opposite case of θ approaching ψ from above, one observes a gradual elongation of a spherical droplets into the directions of the wedge bottom. Eventually, in the limit $\theta = \psi$, the liquid extends to the entire wedge, and the liquid-vapor interface attains a plane configuration (6). Kitron-Belinkov et al. (60) discuss effects to be expected for a finite curvature of the wedge bottom.

Shuttleworth & Bailey (61) were the first to note that the tip of a liquid filament becomes more and more pointed as the contact angle reaches the wedge angle. One of their central assumptions is that the liquid-vapor interface close to the tip becomes asymptotically plane. On the basis of this assumption, they introduced a slope angle β between the free liquid interface and the bottom
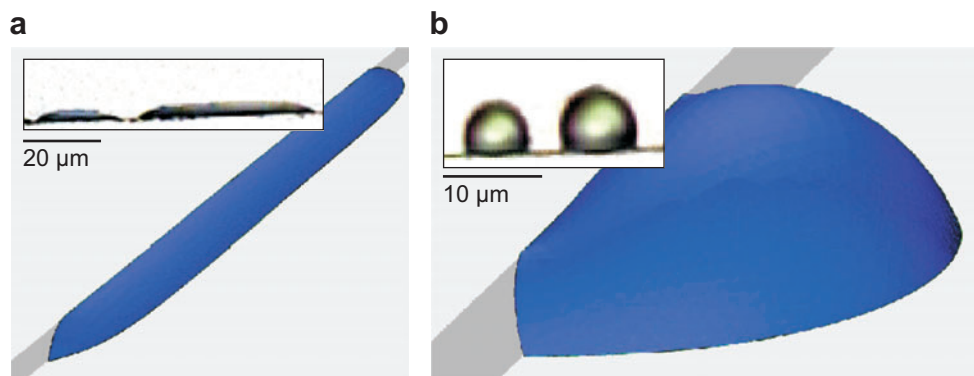
Figure 4

(*a*) Slope angle β at the liquid tip for different contact angles θ. Data points were obtained from experiments with polystyrene droplets (PS) and from electrowetting experiments (EW). The dashed curve displays the theory of Shuttleworth & Bailey (61) according to Equation 6 for a wedge angle of $\psi = 54.7°$. (*b*) AFM micrograph of the terminal meniscus of a polystyrene droplet in a triangular groove illustrating the definition of the slope angle β.

of the wedge and derived relations

$$\cos\beta \ \cos\psi = \cos\theta \quad \text{and} \quad \tan\phi \ \tan\theta = \tan\beta, \qquad 6.$$

which can be applied in the range of contact angles above the wedge angle. The slope angle β and the opening angle of the projected tip ϕ approach zero as the contact angle θ tends to the wedge angle ψ (6, 61). Equation 6 is experimentally confirmed by measurements of the slope angle β and opening angle ϕ in triangular grooves as a function of the contact angle θ (see **Figure 4**).

The central assumption of Shuttleworth & Bailey (61) was later corroborated by Concus & Finn (62), who showed that any surface of zero mean curvature that forms a constant contact angle

a

20 µm

b

10 µm

Figure 5

Numerically computed liquid filament (*a*) and droplet (*b*) wetting a topographic step with a step angle of
$\alpha = 110°$. The volume and contact angle are $V/h^3 = 25$ and $\theta = 40°$ for both morphologies. (*Insets*) Optical
micrographs of polystyrene wetting a step with (*a*) height $h \approx 780$ nm and contact angle $\theta \approx 41°$ and
(*b*) $h \approx 700$ nm, $\theta \approx 76°$.

with the walls of an infinite wedge has to be a plane. Because the shape of an infinite wedge is scale
invariant, one may argue that the tip of any constant mean curvature surface approaches a surface
of zero mean curvature when viewed on an increasingly small length scale. These observations
imply that the very tip of any static liquid morphology in an ideal wedge is asymptotically plane.

The complexity of the wedge geometry can be further increased by adding new corners and
edges. A topographic step represents the most fundamental topography beyond the infinite wedge,
as sketched in **Figure 2d**. A topographic step is characterized by a step angle α and a step height h. In
contrast to the infinite wedge geometry, the liquid volume represents a relevant control parameter
of equilibrium shapes wetting a topographic step: The step height h provides an additional length
scale besides the natural length scale $\propto V^{1/3}$ for a given liquid volume V. For small volumes and
for sufficiently small contact angles, however, one expects to find liquid morphologies identical to
those of the infinite wedge.

If the contact angle exceeds the step angle and if, in addition, the volume of the liquid is
sufficiently large, the liquid will explore the finite vertical extension of the step. The contact line
of the latter morphologies will be pinned to the upper, acute edge of the step. This allows the
liquid to form elongated filaments of homogeneous cross section and positive Laplace pressure
wetting a finite section of the step (35). The filaments in an infinite wedge wet the entire wedge
bottom and exhibit a negative Laplace pressure throughout. Such liquid filaments with a positive
Laplace pressure will be found in the rather narrow range of contact angles $45° < \theta < 54.5°$ at a
rectangular step (35). These filaments are metastable with respect to droplets whose contact line is
pinned to the acute edge of the step. **Figure 5** illustrates both types of morphologies, as obtained
from numerical minimization and observed in wetting experiments.

4.2. Linear Surface Grooves

The next two fundamental linear surface topographies following the infinite wedge and step are
given by symmetric grooves with triangular cross section and rectangular cross section, respectively
(see **Figure 2e, f**). For later convenience we use the width of the groove, w, and the wedge angle
ψ to characterize the surface geometry quantitatively. The distance between two neighboring
grooves is assumed to be larger than the dimensions of the wetting morphologies. In other words,
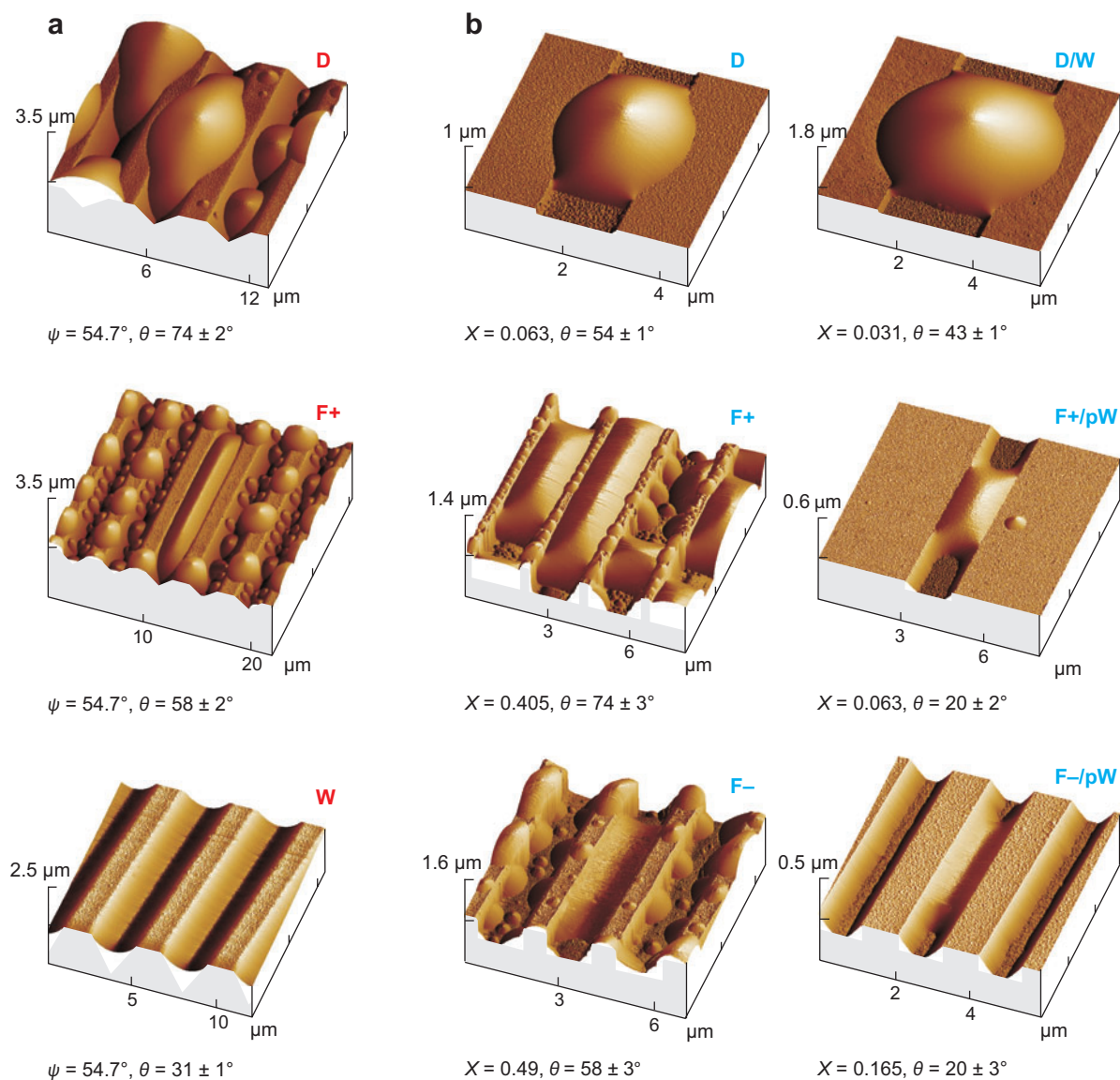we consider only morphologies wetting a single groove.

The spectrum of liquid equilibrium shapes in a triangular groove is basically identical to that of a topographic step: We find elongated liquid filaments (F) of finite length and positive Laplace pressure and almost spherical "overspilling" droplets (D), wetting the groove and the plane parts of the substrate to either sides of the groove. In the range of contact angles θ that are lower than the wedge angle ψ, the bottom of a triangular groove is completely wet by a single liquid filament (W) with negative Laplace pressure. The contact line of the latter is located on the side walls of the groove. Only at large filling degrees may the contact line become pinned to the upper groove edges for $\theta < \psi$. The series of AFM micrographs depicted in **Figure 6a** shows the three principal equilibrium shapes in triangular grooves observed after condensation of polystyrene from the vapor phase onto the sample. The appearance of certain equilibrium shapes is illustrated best in the form of morphology diagrams, as shown in **Figure 7**.

To illustrate the hysteresis of the transitions between filaments (F) and droplets (D), let us conduct a thought experiment: We start with a lemon-shaped droplet (D) and decrease the contact angle. The liquid inside the droplet becomes completely sucked into the groove and forms a filament (W) with negative Laplace pressure at the time that the value of contact angle falls below the purple line in **Figure 7a**. While the contact angle is slowly increased back to its original value, the filament will first undergo a continuous transition into an elongated filament (F) with positive Laplace pressure and finite extension at the solid line, followed by a discontinuous transition into a droplet morphology (D) on the gold line of the morphology diagram in **Figure 7a**. In the region of contact angles above the gold line, liquid filaments (F) and droplets (D) can be found as local minima of the interfacial energy. In conclusion, the appearance of the droplets as well as that of the filaments depend on the history of the control parameter.

Static liquid morphologies found in or on rectangular grooves are similar to those of triangular grooves but differ in some essential details (4, 6). A rectangular groove can be regarded as an antisymmetric combination of two topographic steps, each with a step angle of $\alpha = \pi/2$. In the limit of large wall-to-wall separation, one may consider a rectangular groove as two individual steps being wet by independent liquid morphologies. However, it becomes likely that liquid structures with a single meniscus spanning between the upper edges of the groove appear as the aspect ratio $X = h/w$ of groove depth h to groove width w increases. It is the interplay of liquid configurations with a single meniscus and configurations with two separate menisci that is responsible for the enlarged spectrum of morphologies (4).

The most prominent liquid equilibria in linear grooves of rectangular cross section are again droplet-like shapes competing with filamentous structures. A compilation of experimental results and numerical minimizations is shown in the lower middle and right columns of **Figure 7**. We find filaments with a single meniscus and of finite length but with either a positively (F+) or a negatively (F−) curved meniscus. The corresponding filament morphology in triangular grooves, i.e., a filament (F) wetting a finite fraction of the groove, must have a positive Laplace pressure. Again, the cross section of the latter type of filaments is independent of the liquid volume, provided that the filament does not experience the finite length of the groove. Hence, any increase in the liquid volume must be accompanied by an increase in the filament length.

A new class of liquid morphologies appears in connection to the wedge geometry formed by the bottom edges of a rectangular groove: The liquid may protrude as fine liquid filaments (W) into the edges to either side of the main liquid morphology. Ideally, the entire length of both bottom edges is wet by liquid. This phenomenon has been observed in experiments for liquid filaments and for droplet-like morphologies. As one moves along the grooves, the contour of the free liquid interface in a perpendicular cut may change from a single meniscus in the main liquid morphology to two menisci in the extending filaments. In accordance with the filling transition at $\theta = \psi$ of an infinite wedge, the wetting phenomenon appears only for contact angles below 45°.

a

D
$\psi = 54.7°, \theta = 74 \pm 2°$

F+
$\psi = 54.7°, \theta = 58 \pm 2°$

W
$\psi = 54.7°, \theta = 31 \pm 1°$

b

D
$X = 0.063, \theta = 54 \pm 1°$

D/W
$X = 0.031, \theta = 43 \pm 1°$

F+
$X = 0.405, \theta = 74 \pm 3°$

F+/pW
$X = 0.063, \theta = 20 \pm 2°$

F−
$X = 0.49, \theta = 58 \pm 3°$

F−/pW
$X = 0.165, \theta = 20 \pm 3°$

Figure 6

AFM scans of different wetting morphologies at different values of the contact angle θ for (*a*) triangular grooves with wedge angle $\psi = 54.7°$ and (*b*) rectangular grooves of various aspect ratios X. The droplets were obtained through condensation of polystyrene on chemically modified silicon substrates. In both geometries one finds extended liquid filaments (F), which are fully confined to the grooves, and droplet-like shapes (D). Filaments with negative Laplace pressure and finite length (F−) are absent in grooves of triangular cross section.

For large volumes $V \gg w^3$ but still smaller than $L w^2$, where L is the length of a groove, the liquid morphologies in rectangular grooves are essentially determined by Young's contact angle θ of the substrate and the aspect ratio X. Hence, we can draw a two-dimensional morphology diagram that maps the experimentally observed and theoretically predicted droplet shapes to the space of control parameters θ and X (4).
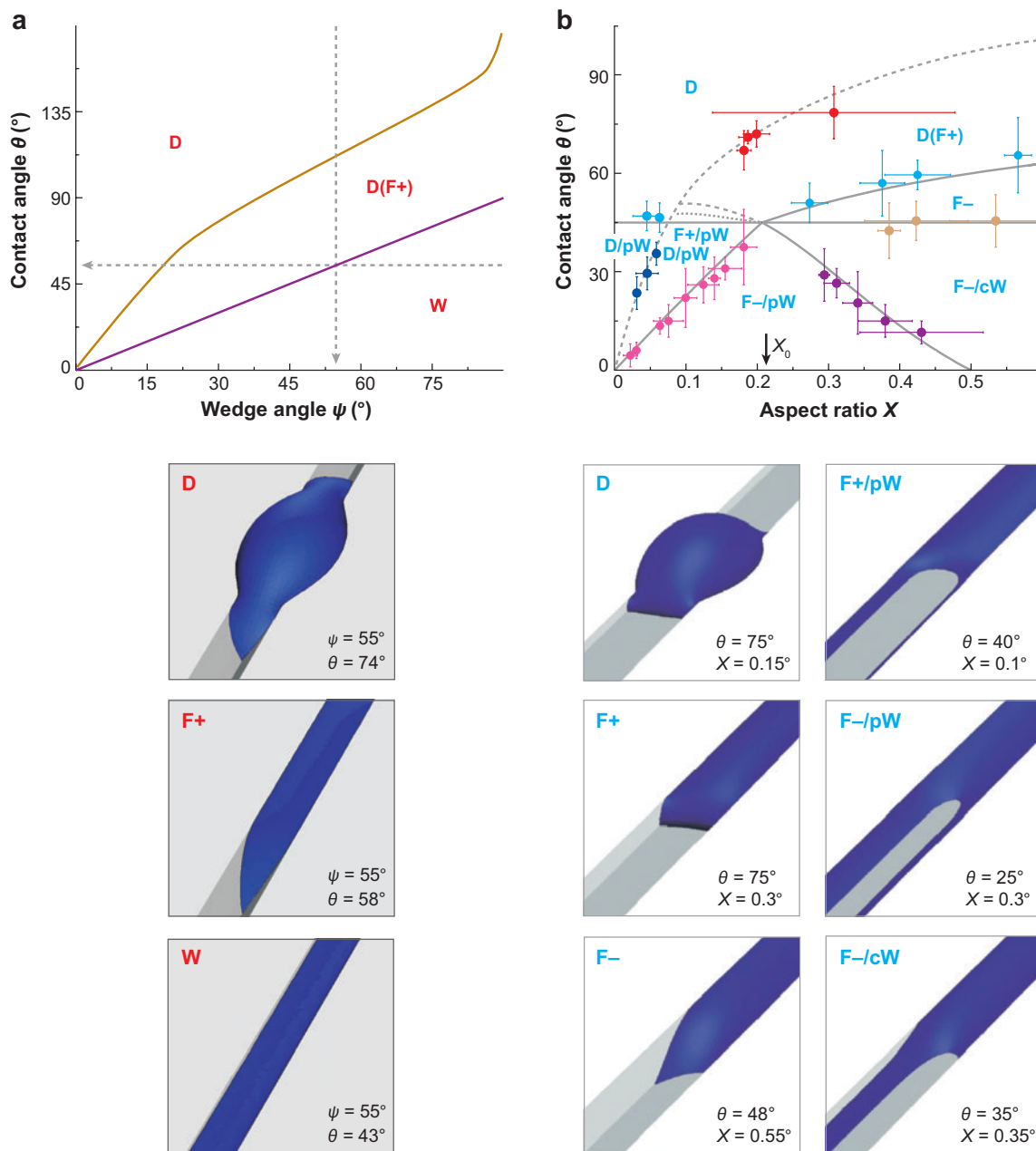
Figure 7

Morphology diagrams (*top*) and numerically obtained droplet shapes (*bottom*) for (*a*) triangular grooves and (*b*) rectangular grooves. In the particular case of triangular grooves, the morphology diagram in panel *a* displays regions of the contact angle θ and the wedge angle ψ where certain equilibrium droplet shapes are locally or globally stable. In the considered regime of moderately large volumes $V \gg w^3$ and $V < w^3 L$ with the length of the groove, L, all liquid filaments with positive Laplace pressure (F) are metastable with respect to droplets (D). The purple line in panel *a* separates the regions where droplets (D) or liquid filaments (W) with negative Laplace pressure are global minima of the interfacial energy. This transition line is simply given by $\theta = \psi$. The gold line bounds the region of control parameter where filaments (F) are found as metastable minima toward large contact angles. Brackets denote metastability of a morphology in the respective region of the diagram.

This morphology diagram is shown in **Figure 7b**. It contains basically the same wetting morphologies that have been identified for triangular grooves and for the topographic step: (*a*) droplets (D) and (*b*) liquid filaments of finite extension with laterally pinned contact lines with either positive (F+) or negative (F–) Laplace pressure. The latter morphologies are separated by a transition line

$$\theta_0 = \arccos\left(\frac{1 - X^2}{1 + X^2}\right). \qquad 7.$$

All wetting morphologies in rectangular grooves, i.e., the filaments (F+) and (F–) and droplets (D) can be found in coexistence with thin liquid filaments (W) wetting the bottom edges of the groove on the same sample. Here, two classes of thin liquid filaments can be distinguished: One of the two contact lines is pinned to the upper edge of the groove (pW), or both contact lines are located on the side walls (cW). **Figure 6b** reveals that thin liquid filaments (cW) can be found in connection with metastable filament morphologies (F+) for contact angles above $\pi/4$. In sufficiently deep grooves $X < 0.5$, however, only thin liquid filaments (cW) in combination with filaments (F–) appear below the line $\theta = 45°$.

5. GROOVE FILLING AND DRAINING

5.1. Electrowetting Experiments

Liquid is spontaneously drawn into the surface grooves from a large droplet (D) when the material contact angle θ of the substrate reaches a certain threshold value θ_0. This value equals simply the wedge angle ψ for grooves of triangular cross section. In the case of rectangular grooves, spontaneous invasion occurs at a contact angle corresponding to the transition line between droplets (D) and liquid filaments with negative Laplace pressure (F–) that is given by Equation 7.

The series of optical micrographs in **Figure 8a** and **b** illustrates advancing liquid filaments in a typical filling transition of triangular and rectangular surface grooves (6, 57). Here, the electrowetting effect on a dielectric insulating layer provides active control of the contact angle (63). In the electrowetting experiments, aqueous salt solution is used as an electrically conductive
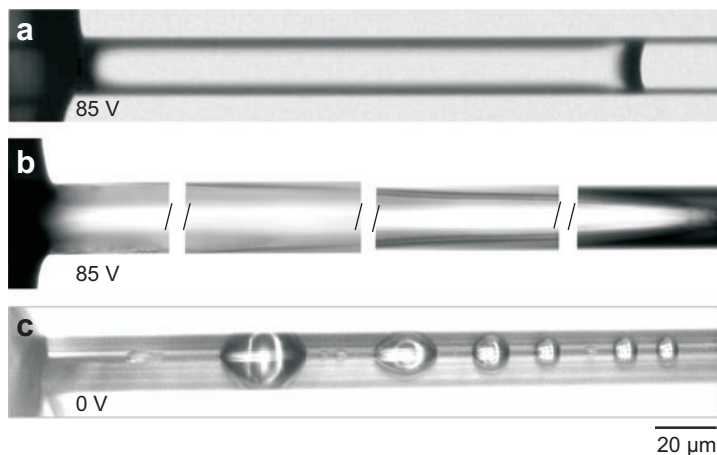
Figure 8

Comparison of electrowetting-induced filling of grooves with (*a*) rectangular cross section and (*b*) triangular cross section. The filling of rectangular grooves (*a*) is fully reversible. In contrast, the liquid filament shown in panel *b* decays into a chain of isolated droplets (*c*) when the voltage is suddenly switched to zero.

wetting liquid. Applying an AC voltage between liquid and the conductive substrate (silicon wafer) lowers the apparent contact angle. Simultaneously, the length of the liquid filament protruding from the large feeding drop is monitored with a digital camera. Owing to the slanted liquid-air interface, the tip of the liquid filament appears black in the micrographs (57).

The electrowetting experiments show a clear threshold contact angle for the filling of the rectangular groove that is in agreement with the morphology diagram in **Figure 7b**, i.e., with Equation 7. The filling transition of rectangular grooves is fully reversible provided that the filaments stay in contact with the large drop. Because the diameter of the feeding drop is larger than the transverse dimensions of the groove, the Laplace pressure can be regarded as being virtually zero. A shape hysteresis is observed only after the complete drop has transformed into a filament (F–). To switch back into a droplet, the contact angle has to be raised above the upper line in the phase diagram in **Figure 7b**, representing the limit of locally stable filaments with positive Laplace pressure (F+).

Assuming that groove filling is solely governed by the pressure difference between the large feeding drop and the filaments, one would expect the filaments to grow indefinitely into the grooves once the filling threshold has been reached. However, the experiments show a dependence of the filament length on the applied voltage and its frequency, and on the conductivity of the liquid (6, 57). This effect can be understood from the voltage drop along the liquid filament. In rectangular grooves, this dependence of the voltage on the lateral position is well described by a transmission line model that considers the filament to be a conducting material of constant cross section surrounded by an insulating layer (63). The filling condition and the Lippmann equation determine the voltage at the tip of the filament. Hence, the voltage at the large feeding drop has to exceed the voltage at the tip to protrude a filament of finite length. Exact solutions of the voltage profile in rectangular grooves yield the filament length as a function of the applied voltage, the electrical conductivity of the liquid, and the capacitance of the dielectric layer (6, 57).

Similar experiments performed with grooves of triangular cross section, however, do not agree with the assumption of homogeneous filaments. Close inspection of several optical micrographs revealed that the cross section of a liquid filament in a triangular groove varies slowly between the tip and the feeding drop (see **Figure 8b**). This is in sharp contrast to a filament in a rectangular groove, whose cross section is homogeneous except for a short region close to the liquid tip. The extension of this transition region between the completely dry and the filled groove is of the order of the groove width, as predicted by theory (6).

The optical image at the top of **Figure 8b** demonstrates that the contact line of the filament is not pinned and instead is located on the side walls of the triangular grooves. This observation is in accord with theoretical arguments given by Shuttleworth & Bailey (61), as discussed in Section 4.1, above. Because the liquid in the groove stays connected to a large feeding drop, it is reasonable to expect a vanishing Laplace pressure inside the filaments. In a first approximation, one may assume that a contact angle of the filament is independent of the lateral position. Then, Equation 6 should describe the geometry of the tip. A solution of the full problem is far more complicated than for the rectangular geometry: The local contact angle depends on the local voltage, which, in return, depends on the geometry of the filament. The latter is fixed by the variation of the contact angle along the filament. Qualitative arguments show that the liquid filament becomes more pointed toward the tip, in accordance with experimental observations (6).

5.2. Filament Instability

Liquid filaments in triangular grooves with a positively curved free liquid interface and non-pinned contact line represent mechanically unstable equilibrium shapes. The latter morphology
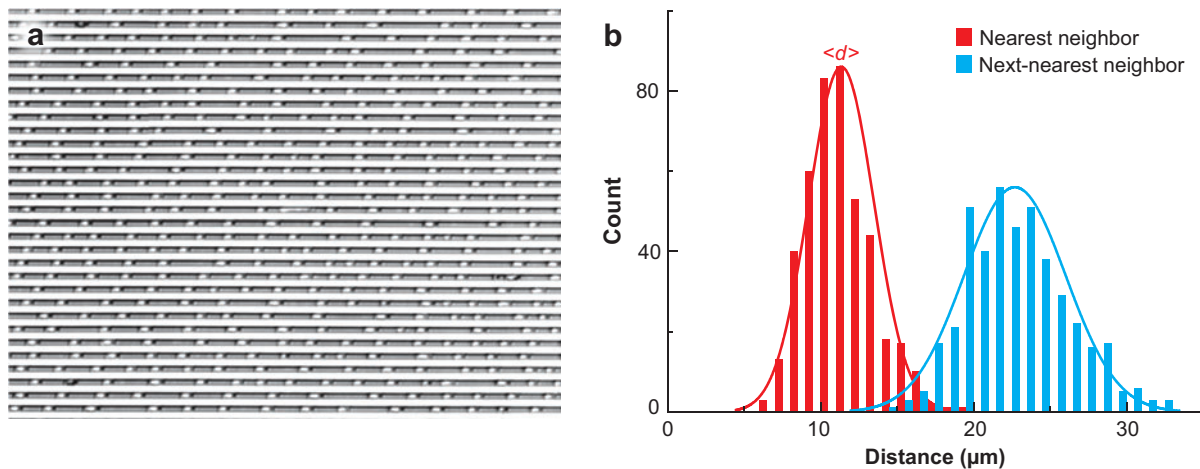
Figure 9

(*a*) Final droplet pattern following the instability of positively curved polystyrene filaments in triangular grooves. (*b*) Distribution of center-to-center distances *d* of neighboring droplets in a groove. ⟨*d*⟩ denotes the preferred separation distance.

can be experimentally obtained as a transient shape if the contact angle is rapidly changed from a value smaller than the wedge angle to a value larger than the wedge angle. **Figure 8c** shows the final state after a rapid quench from a stable liquid filament (**Figure 8b**) into an unstable configuration. The contact angle was suddenly ramped up by switching off the voltage. As a result, the filament becomes unstable and decays in a characteristic way into a chain of isolated droplets.

The dynamics of the filament decay has been studied in more detail on the micrometer scale (5): Triangular grooves etched into a silicon wafer were covered with silanes to modify the wettability. Polystyrene was spin cast from toluene solution onto the grooved substrates, forming a thin glassy polymer film on the surface. As the solvent evaporated during the spin coating process, the polymer froze in a nonequilibrium morphology, forming filaments with polymer-vapor interface curved toward the wedge bottom. When heated to more than the glass transition temperature, the liquid polystyrene very rapidly restored its material contact angle with the coated substrate. The cross section of the polystyrene-air interface relaxed toward a circular arc, curved toward the vapor phase, and remained homogeneous immediately after melting.

For all contact angles, we observed that the timescale related to the longitudinal reorganization into liquid droplets exceeded the timescale of this transverse equilibration by orders of magnitude. Different surface coatings allowed tuning of the contact angle between ≈55° and ≈75° (5). Deviations of the contact angle from the static value during the decay of the filaments remained less than ≈2° (5). This corroborates the observation that, in many systems, contact angle hysteresis seems to be only a minor influence on a length scale of a few micrometers (4).

The optical micrograph in **Figure 9** shows the final pattern of polystyrene droplets after the filament decay. As shown in **Figure 9b**, the distribution of droplet separations is well described by a Gaussian. The variance of the distribution is in the range of 20% of the preferred separation distance ⟨*d*⟩. The latter is obtained by averaging over all droplet center-to-center distances of the final state.

The basic mechanism for the filament instability is related to the Rayleigh-Plateau instability of a freestanding liquid cylinder (64). If the contact angle exceeds the wedge angle, an increase in the filling reduces the Laplace pressure and drives the liquid from regions with smaller filling

height toward regions with larger filling height, resulting in an instability. Very short corrugations are effectively suppressed by an additional curvature into the direction of the grooves, but all fluctuations above a certain critical longitudinal wavelength λ^* are amplified. Because viscous resistance suppresses liquid flux over large distances, we find a wavelength $\lambda_{max} > \lambda^*$ for which the growth rate is maximal. Experimental results clearly show that this preferred wavelength prevails in the spatial pattern until the very late stages of the dewetting process (5, 6).

6. SUPERHYDROPHOBIC SUBSTRATES

Substrate geometries with a particular wetting behavior are obtained when two periodic arrays of linear grooves into different directions are superimposed. Liquid morphologies characteristic of linear surface grooves are encountered if the distance between the individual grooves is larger than the groove width. Substantially new classes of droplet shapes, however, are observed in, or close to, the crossing points of the grooves, in particular when the size of the posts becomes comparable to the groove width (7, 8). A rich spectrum of liquid shapes unfolds in and on the substrate topographies once the droplets grow and coalesce, which is accompanied by reorganizations into larger and more complex droplet morphologies (7, 8).

Small-scale surface topographies such as, for example, a periodic array of square posts can lead to an enormous enhancement of hydrophobicity (15). Barthlott & Neinhuis (1) first reported the relation between high contact angles and microscopic surface topographies found on Lotus leaves and a variety of other plants. Onda et al. (65) carried out the first systematic study of an artificial superhydrophobic surface, employing alkylketene dimer crystals as topographic features, which resulted in a reproducible roughness.

Wenzel's equation (6) cannot be used to explain the superhydrophobic effect (16, 66): The absolute of the roughness factor that appears in this equation must not become larger than $|1/\cos\theta|$ because the cosine of the apparent contact angle is limited to the interval $[-1, 1]$. The basic assumption of Wenzel's approach is clearly invalidated by a superhydrophic droplet state: Owing to air entrainment the liquid is not in full contact with the hydrophobic substrate. The presence of patches of liquid-air interface at the bottom of a droplet can be directly inferred from the silver or shiny white color caused by the total internal reflection. These patches of liquid-air interface can be viewed as virtually belonging to a substrate with a contact angle of $\theta = 180°$ (16).

Periodic arrays of identical posts are ideal systems to study the transition between the normal wetting state and the superhydrophobic state (15, 67). Such types of substrates can be easily obtained by standard photolithographic methods or by micromachining, as outlined in Section 3. A major advantage is their well-defined geometry: The ideally plane top of the posts allows one to compute the transition of the normal hydrophobic, or Wenzel, regime to the superhydrophobic Cassie state because the liquid-air interface is pinned to the edges of the posts and, hence, will be plane. Bico et al. (66) compared the energies of the wetting states in both regimes and found that the transition between the Wenzel state and the superhydrophobic state occurs at a Young's contact angle θ_c that is given by

$$\cos\theta_c = -\frac{1 - \phi_s}{r - \phi_s}. \qquad 8.$$

Here, ϕ_s denotes the area fraction of the posts relative to the total area of the substrate, whereas r is the roughness of the substrate. As shown in Reference 15, both the superhydrophobic state and the Wenzel state can survive as metastable states at values $\theta < \theta_c$ and $\theta > \theta_c$, respectively, of Young's angle θ. The energetic barrier between the two states may depend strongly on the geometry of the surface geometry.

Lafuma & Quéré (15) demonstrated that the transition between the two wetting states can be triggered by changes in the Laplace pressure. An increase in the Laplace pressure of the wetting droplet and air can be reached by squeezing the droplets between two substrates or while the size of the droplets decreases during evaporation. Another method to increase the (local) pressure difference between liquid and air is to let a droplet fall onto the substrate. In all three cases, one observes a threshold for imbibition, i.e., for a transition into the Wenzel state.

The condensation and growth of liquid droplets on a superhydrophobic surface and the possibility for transitions from the Wenzel state to the Cassie state have been studied experimentally and theoretically (7, 8). Experiments using arrays of square posts of high aspect ratios as superhydrophobic substrates have revealed the complex and rich behavior of morphological transitions and coalescence events of the growing droplets.

Surprisingly, the underlying substrate material need not be hydrophobic to create a superhydrophobic surface. Herminghaus (3) has discussed the possibility of constructing such a surface geometry. Furthermore, Otten & Herminghaus (9) demonstrated that the carpet of slightly hydrophilic hair (contact angle $\theta \approx 60°$) on the leaves of the plant Lady's mantle (*Alchemilla vulgaris*) prevents large water droplets from touching the actual surface of a leaf. A pair of neighboring hairs that partially stick into the water droplet bundles in the air-water interface by means of an attractive capillary interaction (68). If the droplet is now pushed toward the leaf surface, the hairs in the bundle start to bend. The smaller the separation of the interface to the leaf surface, the stronger the curvature of the hair is. A repulsive force arises because the deformation of the hair is related to an increase in elastic energy (9).

7. OUTLOOK

We have seen that rather simple topographic structures may render the wettability of a surface amazingly complex. Not only is there frequently no unique stable liquid morphology, but several different ones may coexist in a wide range of parameters on the same sample. Transitions between them may exhibit symmetry-breaking phenomena, similar to the Rayleigh-Plateau instability. When one aims to describe liquids at substrates of even higher complexity, such as, e.g., biological surfaces, one is faced with a richness of phenomena that at first glance seems unmanageable. However, we have seen that owing to the smallness of the involved structures, some exacerbating (and poorly understood) effects known from the larger scale, such as unintentional contact line pinning and contact angle hysteresis, seem to play a minor role in this context. Consequently, one may expect that simple theoretical concepts of wetting, as we use here for describing some paradigm systems, can be successfully applied to tackle more complex topographies as well. A complete understanding of the statics and dynamics of wetting on complex substrate structures thus seems to be a matter of commitment rather than a matter of lacking physical concepts.

DISCLOSURE STATEMENT

The authors are not aware of any biases that might be perceived as affecting the objectivity of this review.

ACKNOWLEDGMENTS

LITERATURE CITED

1. Barthlott W, Neinhuis C. 1997. Purity of the sacred lotus, or escape from contamination in biological surfaces. *Planta* 202:1–8
2. Blossey R. 2003. Self-cleaning surfaces: virtual realities. *Nat. Mater.* 2:301–6
3. Herminghaus S. 2000. Roughness-induced non-wetting. *Europhys. Lett.* 52:165–70. Erratum. 2007. *Europhys. Lett.* 79:59901
4. Seemann R, Brinkmann M, Lange FF, Kramer EJ, Lipowsky R. 2005. Wetting morphologies at microstructured surfaces. *Proc. Natl. Acad. Sci. USA* 102:1848–52
5. Khare K, Brinkmann M, Law BM, Gurevich E, Herminghaus S, Seemann R. 2007. Dewetting of liquid filaments in wedge-shaped grooves. *Langmuir* 23:12138–41
6. Khare K, Law BM, Herminghaus S, Brinkmann M, Seemann R. 2007. Switching liquid morphologies on linear grooves. *Langmuir* 23:12997–13006
7. Narhe RD, Beysens DA. 2007. Growth dynamics of water droplets on a square-pattern rough hydrophobic substrate. *Langmuir* 23:6486–89
8. Dorrer C, Rühe J. 2007. Condensation and wetting transitions on microstructured ultrahydrophobic surfaces. *Langmuir* 23:3820–24
9. Otten A, Herminghaus S. 2004. How plants keep dry: a physicist's point of view. *Langmuir* 20:2405–8
10. Sun TL, Feng L, Gao XF, Jiang L. 2005. Bioinspired surfaces with special wettability. *Acc. Chem. Res.* 38:644–52
11. Hauck M, Jürgens SR, Brinkmann M, Herminghaus S. 2008. Surface hydrophobicity causes SO_2 tolerance in lichens. *Ann. Bot.* 101:531–39
12. Shirtcliffe NJ, Pyatt FB, Newton MI, McHale G. 2006. A lichen protected by a superhydrophobic and breathable structure. *J. Plant Physiol.* 163:1193–97
13. Feng XQ, Gao XF, Wu ZN, Jiang L, Zheng QS. 2007. Superior water repellency of water strider legs with hierarchical structures: experiments and analysis. *Langmuir* 23:4892–96
14. Cao A, Cao L, Gao D. 2007. Fabrication of nonageing superhydrophobic surfaces by packing flowerlike hematite particles. *Appl. Phys. Lett.* 91:034102
15. Lafuma A, Quéré D. 2002. Superhydrophobic states. *Nat. Mater.* 2:457–60
16. Quéré D. 2005. Non-sticking drops. *Rep. Prog. Phys.* 68:2495–532
17. Lipowsky R, Lenz P, Swain PS. 2000. Wetting and dewetting of structured and imprinted surfaces. *Colloids Surf. A* 161:3–22
18. Checco A, Gang O, Ocko BM. 2006. Liquid nanostripes. *Phys. Rev. Lett.* 96:056104
19. Checco A, Cai YG, Gang O, Ocko BM. 2006. High resolution noncontact AFM imaging of liquids condensed onto chemically nanopatterned surfaces. *Ultramicroscopy* 106:703–8
20. Parry AO, Rascon C, Wood AJ. 2000. Critical effects at 3D wedge wetting. *Phys. Rev. Lett.* 85:345–48
21. Rascon C, Parry AO. 2000. Geometry-dominated fluid adsorption on sculpted solid substrates. *Nature* 407:986–89
22. Rowlinson JS, Widom B. 1982. *Molecular Theory of Capillarity*. Calderon: Oxford Univ. Press
23. de Gennes PG. 1985. Wetting: statics and dynamics. *Rev. Mod. Phys.* 57:827–63
24. Herminghaus S, Jacobs K, Mecke K, Bischof J, Fery A, et al. 1998. Spinodal dewetting in liquid crystals and liquid metal films. *Science* 282:916–19
25. Becker J, Grün G, Seemann R, Mantz H, Jacobs K, et al. 2003. Complex dewetting scenarios captured by thin-film models. *Nat. Mater.* 2:59–63
26. Bauer C, Dietrich S, Parry AO. 1999. Morphological phase transitions of thin fluid films on chemically structured substrates. *Europhys. Lett.* 47:474–80
27. Dobbs H. 1999. The elasticity of a contact line. *Physica A* 271:36–47
28. Seemann R, Jacobs K, Blossey R. 2001. Polystyrene nanodroplets. *J. Phys. Condens. Matter* 13:4915–23
29. Fery A, Reim D, Herminghaus S. 1997. Imaging of droplets of aqueous solutions by tapping-mode scanning force microscopy. *Ultramicroscopy* 69:211–17
30. Do Carmo MP. 1976. *Differential Geometry of Curves and Surfaces*. New Jersey: Prentice Hall
31. Cassie ABD. 1948. Contact angles. *Disc. Faraday Soc.* 3:11–16
32. Wenzel TN. 1949. Surface roughness and contact angle. *J. Phys. Colloid Chem.* 53:1466–67

33. Swain PS, Lipowsky R. 1998. Contact angles on heterogeneous surfaces: a new look at Cassie's and Wenzel's laws. *Langmuir* 14:6772–80

34. Dorrer C, Rühe J. 2007. Contact line shape on ultrahydrophobic post surfaces. *Langmuir* 23:3179–83

35. Brinkmann M, Blossey R. 2004. Blobs, channels and "cigars": morphologies of liquids at a step. *Eur. Phys. J. E* 14:79–89

36. Ondarcuhu T, Piednoir A. 2005. Pinning of a contact line on nanometric steps during the dewetting of a terraced substrate. *Nano Lett.* 5:1744–50

37. Brakke KA. 1992. The surface evolver. *Exp. Math.* 1:141–65

38. Brakke KA. 1996. The surface evolver and the stability of liquid surfaces. *Philos. Trans. R. Soc. London Ser. A* 354:2143–57

39. Mann JA, Romero L, Rye RR, Yost FG. 1995. Flow of simple liquids down narrow *V* grooves. *Phys. Rev. E* 52:3967–72

40. Rye RR, Yost FG, Mann JA. 1996. Wetting kinetics in surface capillary grooves. *Langmuir* 12:4625–27

41. Rye RR, Mann JA, Yost FG. 1996. The flow of liquids in surface grooves. *Langmuir* 12:555–65

42. Yost FG, Rye RR, Mann JA. 1997. Solder wetting kinetics in narrow V-grooves. *Acta Mater.* 45:5337–45

43. Bruschi L, Carlin A, Mistura G. 2002. Complete wetting on a linear wedge. *Phys. Rev. Lett.* 89:166101

44. Chou SY, Krauss PR, Renstrom PJ. 1995. Imprint of sub-25 nm vias and trenches in polymers. *Appl. Phys. Lett.* 67:3114–16

45. Chou SY, Krauss PR, Renstrom PJ. 1996. Imprint lithography with 25-nm resolution. *Science* 272:85–87

46. Haisma J, Verheijen M, van den Heuvel K, van den Berg J. 1996. Mold-assisted nanolithography: a process for reliable pattern replication. *J. Vac. Sci. Technol. B* 14:4124–28

47. Heckele M, Bacher W, Muller KD. 1998. *Microsyst. Technol.* 4:122–24

48. Bender M, Otto M, Hadam B, Vratzov B, Spangenberg B, Kurz H. 2000. Fabrication of nanostructures using a UV-based imprint technique. *Microelectron Eng.* 53:233–36

49. Colburn M, Grot A, Choi BJ, Amistoso M, Bailey T, et al. 2001. Patterning nonflat substrates with a low pressure, room temperature, imprint lithography process. *J. Vac. Sci. Technol. B* 19:2162–72

50. Otto M, Bender M, Hadam B, Spangenberg B, Kurz H. 2001. Characterization and application of a UV-based imprint technique. *Microelectron Eng.* 57:361–66

51. Chou SY, Keimel C, Gu J. 2002. Ultrafast and direct imprint of nanostructures in silicon. *Nature* 417:835–37

52. Xia YN, Whitesides GM. 1998. Soft lithography. *Annu. Rev. Mater. Sci.* 28:153–84

53. Gates BD, Xu QB, Stewart M, Ryan D, Willson CG, Whitesides GM. 2005. New approaches to nanofabrication: molding, printing, and other techniques. *Chem. Rev.* 105:1171–96

54. Seemann R, Kramer EJ, Lange FF. 2004. Patterning of polymers: precise channel stamping by optimizing wetting properties. *New J. Phys.* 6:111

55. Kim MJ, Song S, Kwon SJ, Lee HH. 2007. Trapezoidal structure for residue-free filling and patterning. *J. Phys. Chem. C* 111:1140–45

56. Madou MJ. 1997. *Fundamentals of Microfabrication*. Boca Raton, LA: CRC Press

57. Baret JC, Decré M, Herminghaus S, Seemann R. 2005. Electroactuation of fluid using topographical wetting transitions. *Langmuir* 21:12218–21

58. Chung JY, Youngblood JP, Stafford CM. 2007. Anisotropic wetting on tunable microwrinkled surfaces. *Soft Matter* 3:1163–69

59. Ming W, Wu D, van Benthem R, de Wirth G. 2005. Superhydrophobic films from raspberry-like particles. *Nano Lett.* 5:2298–301

60. Kitron-Belinkov M, Marmur A, Trabold T, Dadheech GV. 2007. Groovy drops: effect of groove curvature on spontaneous capillary flow. *Langmuir* 23:8406–10

61. Shuttleworth R, Bailey GLJ. 1948. The spreading of a liquid over a rough solid. *Disc. Faraday Soc.* 3:16–22

62. Concus P, Finn R. 1969. On behavior of a capillary surface in a wedge. *Proc. Natl. Acad. Sci. USA* 63:292–99

63. Mugele F, Baret JC. 2005. Electrowetting: from basics to applications. *J. Phys. Condens. Mater.* 17:R705–74

64. Lord Rayleigh. 1878. On the instability of jets. *Proc. London Math. Soc.* 10:4–13

65. Onda T, Shibuichi S, Satoh N, Tsujii K. 1996. Super-water-repellent fractal surfaces. *Langmuir* 12:2125–27

66. Bico J, Thiele U, Quéré D. 2002. Wetting of textured surfaces. *Colloids Surf. A* 206:41–46

67. Dorrer C, Rühe J. 2006. Advancing and receding motion of droplets on ultrahydrophobic post surfaces. *Langmuir* 22:7652–57

68. Velev OD, Denkov ND, Paunov VN, Kralchevsky PA, Nagayama K. 1993. Direct measurement of lateral capillary forces. *Langmuir* 9:3702–9

$\hat{A}R$

Contents

Current Interest

Index

Errata

An online log of corrections to *Annual Review of Materials Research* articles may be
found at http://matsci.annualreviews.org/errata.shtml